Energy 292 (2024) 130524

Contents lists available at ScienceDirect

Energy

journal homepage: www.elsevier.com/locate/energy

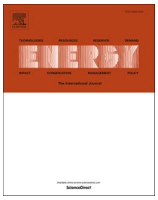

Thermochemical energy storage in $SrCO_3$ composites with $SrTiO_3$ or $SrZrO_3$

Kyran Williamson [a,b,1], Yurong Liu [a,1], Terry D. Humphries [a], Anita M. D'Angelo [c], Mark Paskevicius [a,*], Craig E. Buckley [a]

[a] Department of Physics and Astronomy, Institute of Energy Transition, Curtin University, GPO Box U1987, Perth, 6845, WA, Australia
[b] Centre for Cooperative Research on Alternative Energies (CIC energiGUNE), Basque Research and Technology Alliance (BRTA), Alava Technology Park, Albert Einstein 48, 01510, Vitoria-Gasteiz, Araba, Spain
[c] Australian Synchrotron, 800 Blackburn Rd, Clayton, VIC, 3168, Australia

ARTICLE INFO

Handling editor: L Luo

Keywords:
Thermochemical energy storage (TCES)
Concentrating solar power (CSP)
Energy storage
Strontium carbonate
Strontium titanate
Strontium zirconate

ABSTRACT

Thermochemical energy storage offers a cost-effective and efficient approach for storing thermal energy at high temperature (~1100 °C) for concentrated solar power and large-scale long duration energy storage. $SrCO_3$ is a potential candidate as a thermal energy storage material due to its high energy density of 205 kJ/mol of CO_2 during reversible CO_2 release and absorption. However, it loses cyclic capacity rapidly due to sintering. This study determined that the cyclic capacity of $SrCO_3$ was enhanced by the addition of either reactive $SrTiO_3$ or inert $SrZrO_3$, where the molar ratios of $SrCO_3$ to $SrZrO_3$ were varied from 1:0.125 to 1:1. Thermogravimetric analysis over 15 CO_2 sorption cycles demonstrated that both materials retained ~80 % of their maximum cyclic capacity on the milligram scale. Repeated measurements using gram scale samples revealed a decrease in maximum capacity to 11 % using a sample of $SrCO_3$ – 0.5 $SrZrO_3$ over 53 cycles, while the use of $SrTiO_3$ additives allowed for the retention of 80 % maximum capacity over 55 cycles. These findings highlight the potential of reactive additives in enhancing the performance of thermochemical energy storage systems, while providing valuable insights for the development of cost-effective materials.

1. Introduction

In the pursuit of a sustainable future, the global energy system is transforming to be largely based on renewable energy. Solar energy represents a major component of the renewable energy mix [1]. One of the most promising technologies to achieve the efficient use of solar energy is concentrated solar power (CSP) integrated with thermal energy storage (TES) [2]. During the hours of sunlight, the excess heat produced through the CSP systems is stored in the TES systems. At times of energy demand, the stored heat is released to generate electricity via a heat engine or steam turbine. In this way, a reduction of peak demand and continuous power supply is achieved [3].

There are three types of TES systems: sensible heat storage (SHS), latent heat storage (LHS), and thermochemical heat storage (TCES) [3]. SHS is based on the temperature change of a liquid or solid medium (e.g., water, sand, and molten salts) during heating or cooling. SHS using molten salts (60 % $NaNO_3$: 40 % KNO_3) is currently the only commercially available technology used in CSP plants, however, the disadvantage of this technology is the low energy storage density (413 kJ/kg) and restricted operating temperature (290–565 °C) [3,4]. LHS utilises the latent heat absorbed or released from a material (e.g., miscibility gap alloys) when it undergoes a phase transition from solid to liquid, or liquid to gas [5,6]. LHS systems using phase change materials have the potential to achieve high efficiency as heat transfer occurs almost isothermally during the process. TCES is based on the storage of heat through reversible endothermic/exothermic reaction processes [7]. Among the three TES technologies, TCES is at an early stage of maturity and has the advantages of higher energy density and higher operating temperatures over most SHS and LHS systems [8] and is considered to be particularly suitable for medium and long-term storage [4,9].

In TCES systems designed for integration with CSP plants, solar heat is used to promote the endothermic battery charging step whereby a reactant A is dissociated into products B and C, as shown in Eq. (1). During the discharging step, heat is released in an exothermic reaction between products B and C when they are combined [10].

$$A + \Delta H_r \rightleftharpoons B + C \quad (1)$$

* Corresponding author.
E-mail address: M.Paskevicius@curtin.edu.au (M. Paskevicius).
[1] joint first author.

https://doi.org/10.1016/j.energy.2024.130524
Received 9 August 2023; Received in revised form 18 January 2024; Accepted 29 January 2024
Available online 6 February 2024

where ΔH_r is the reaction enthalpy.

Extensive studies have been carried out on screening of potential TCES materials including metal hydrides [11–14], metal oxides [4], carbonates [15–19], hydroxides [6] and ammonia [3,4]. The metal hydride Mg_2FeH_6 has been shown to cycle hundreds of times, but it's operating temperature is limited to below 600 °C [14], while $CaH_2 + 2Al$ has been shown to cycle 67 times at a maximum temperature of 670 °C For CSP applications [20], higher temperatures are required to increase efficiency. Carbonate-oxide systems can operate at higher temperatures with $CaCO_3$ operating at ~900 °C with high energy densities [10,18,19,21,22]. Among these materials, alkaline earth metal carbonate-oxide systems (MCO_3/MO, with M = Ca, Sr, Ba) are especially attractive due to their abundance, low cost, and non-toxicity. Carbonate-oxide systems are based on the cyclic carbonation/calcination process. During the endothermic reaction (calcination), the carbonate (MCO_3) is decomposed into a metal oxide (MO) and CO_2 gas. The CO_2 is stored until the reverse exothermic reaction is required between MO and CO_2 in the carbonation process.

The $CaCO_3$/CaO system has been heavily investigated for both energy storage [16,17,19,23] and carbon capture applications [24,25]. The $SrCO_3$/SrO system recently gained attention due to its high decomposition temperature (ΔG = 0 kJ/mol at 1175 °C), allowing an increased operating temperature (~1200 °C) than the $CaCO_3$/CaO system (900 °C) [10]. Its high operating temperature also matches the combined Brayton-Rankine cycle, which could increase the overall energy efficiency of the power plants [4,18,26,27]. Moreover, $SrCO_3$ has a high volumetric energy density (4 $GJm^{-3}_{SrCO_3}$), which leads to a reduction in feedstock and therefore a cost reduction for the storage vessel [4]. Despite these favourable features, this system demonstrates thermal sintering problems at high temperature, which has also been observed in the $CaCO_3$/CaO system [28,29].

The sintering and agglomeration of particles at high temperatures causes morphological changes in the material, hindering the absorption of CO_2 by SrO decreasing the CO_2 cyclic capacity over time. Adding sintering-resistant inert additives such as $SrSiO_3$ [18], Al_2O_3 [30], MgO [31], ZrO_2 [21] has proven to be an effective approach to improve the cyclic stability of the $SrCO_3$/SrO system. Addition of $SrSiO_3$ to $SrCO_3$ also thermodynamically destabilises $SrCO_3$ allowing an operating temperature of 700 °C, in turn increasing the potential for industrial application [18]. Here the $SrSiO_3$ reversibly reacts with $SrCO_3$ during CO_2 release forming Sr_2SiO_4. Unfortunately, agglomeration occurs during cycling causing poor cyclability, but addition of 20 wt% NaCl: $MgCl_2$ catalyst to the reactive carbonate composite (RCC) promotes a dramatic increase in the kinetics of absorption and desorption of CO_2 and enables 80 % capacity retention over several cycles. When 34 wt% Al_2O_3 is added to $SrCO_3$, a consistent 11 wt% CO_2 capacity is observed over 5 cycles at 1000 °C although sintering is also observed [30]. Unfortunately, the article focuses on the kinetics of the reaction rather than the processes involved but, it is noted that the $SrCO_3$ and Al_2O_3 react to form strontium aluminium oxide phases that are unlikely to undergo reversible reactions with CO_2 and is the reason for the reduction on CO_2 cyclic capacity. The cycling performance of $SrCO_3$ (40 wt%) was shown to be enhanced by using a wet-mixing method with strontium acetate hemihydrate and porous magnesium oxide with 100 cycles demonstrated at 1000 °C. Amghar et al. studied the effects of adding ZrO_2, MgO and SiO_2 (5 and 10 wt%) to $SrCO_3$ [21]. After 20 cycles a decay in cyclic capacity was observed for each sample, although the SiO_2 samples were the most stable with an effective conversion of 0.22 even after 30 cycles. Strontium silicates and zirconates were observed to form during cycling but MgO was inert during the process.

As the addition of $SrSiO_3$, SiO_2 and ZrO_2 causes the formation of ternary oxides that promote thermodynamic destabilisation and cyclic stability of $SrCO_3$, this study determines the effect of the addition of $SrTiO_3$ and $SrZrO_3$ to $SrCO_3$. The energy storage performance of the proposed systems are experimentally assessed at 1100 °C by thermogravimetric analysis (TGA) and by using Sieverts apparatus [32]. There is one previous study on SrO supported by $SrZrO_3$ for thermochemical energy storage [27]. Rhodes et al. used a mass ratio of 2:3 of $SrO/SrZrO_3$ and cycled between carbonation (1150 °C, $p(CO_2)$ = 1 bar) and calcination (1235 °C, $p(CO_2)$ = 0.1 bar) using thermogravimetric analysis (TGA), however the sample only stabilised at 24 % of the maximum theoretical CO_2 capacity [27]. This work furthers this study by varying the ratios of the $SrZrO_3$ additive and the pressures used during cycling to optimise the CO_2 absorption capacity of SrO. The molar ratios of $SrCO_3$ to $SrZrO_3$ were varied from 1:0.125 to 1:1.

2. Experimental

2.1. Synthesis of $SrTiO_3$ and $SrZrO_3$

$SrTiO_3$ and $SrZrO_3$ were prepared through solid state reaction between $SrCO_3$ (Sigma-Aldrich, >99 %) and TiO_2 (GPR RECTAPUR, ≥99 %) or $SrCO_3$ and ZrO_2 (Aldrich, >99 %). A mixture of $SrCO_3$ and TiO_2 or ZrO_2 in stoichiometric amounts according to Eq. (2) and Eq. (3) were mixed by ball milling for 2 h (6 bidirectional 20 min segments with 1 min breaks) in a planetary type mill (PQ-N04) employing stainless steel (316) milling vials (80 mL) and balls (8 mm in diameter) with a ball to powder mass ratio of 10:1. The powder mixture was then placed in an Al_2O_3 boat in a (Thermo-FB1310 M) furnace and subjected to calcination in an air atmosphere by heating to 1100 °C ($\Delta T/\Delta t$ = 10 °C/min) then held isothermally for 3 h to obtain $SrTiO_3$ and $SrZrO_3$.

$$SrCO_{3(s)} + TiO_{2(s)} \rightarrow SrTiO_{3(s)} + CO_{2(g)} \quad (2)$$

$$SrCO_{3(s)} + ZrO_{2(s)} \rightarrow SrZrO_{3(s)} + CO_{2(g)} \quad (3)$$

2.1.1. Preparation of $SrCO_3$–$SrTiO_3$ and $SrCO_3$–$SrZrO_3$ samples

The $SrCO_3$–$SrTiO_3$ and $SrCO_3$–$SrZrO_3$ composites were prepared by ball milling $SrCO_3$ with synthesised $SrTiO_3$ or $SrZrO_3$ for 1 h (three bidirectional 20-min segments with 1-min breaks) using the aforementioned parameters. Composites with various molar ratios of $SrCO_3$ and $SrZrO_3$, e.g. $SrCO_3$-0.5 M $SrZrO_3$ correspond to a sample with a $SrCO_3$ and $SrZrO_3$ molar ratio of 1:0.5 respectively (See Table 1). As $SrCO_3$–$SrTiO_3$ are expected to react with one another in a 1:1 ratio, the optimum ratio of mixing is 1:1. On the other hand, $SrCO_3$ and $SrZrO_3$ are not expected to react, therefore altering the ratios might affect the kinetics of reaction as well as the maximum CO_2 capacity of the system. As such, these parameters should be optimised as to maximise, operating conditions and cost of materials.

2.2. Thermogravimetric analysis (TGA)

Thermogravimetric analysis (TGA) was performed on a Netzsch STA 449 F3 Jupiter instrument. The samples (15–20 mg) were measured inside Al_2O_3 crucibles with pierced lids and were heated from room temperature to 1200 °C ($\Delta T/\Delta t$ = 10 °C/min) under a flowing argon (Coregas, 99.995 %, 20 mL min^{-1}) atmosphere. The temperature was calibrated using In, Zn, Al, Ag and Au reference materials, resulting in a temperature accuracy of ±0.2 °C, while the balance has an accuracy of ±20 μg.

Table 1
Details of prepared samples.

Samples	$SrCO_3$:$SrTiO_3$/$SrZrO_3$ molar ratio	Theoretical CO_2 wt%
$SrCO_3$	1	29.81
$SrCO_3$ - 1 M $SrTiO_3$	1: 1	13.29
$SrCO_3$ - 1 M $SrZrO_3$	1: 1	11.75
$SrCO_3$ - 0.5 M $SrZrO_3$	1: 0.5	16.85
$SrCO_3$ - 0.25 M $SrZrO_3$	1: 0.25	21.53
$SrCO_3$ - 0.125 M $SrZrO_3$	1: 0.125	25.00

2.3. CO_2 cyclic capacity measurements

An initial assessment of the carbonation/calcination cyclic capacity was performed by TGA (Netzsch STA 449) with calibration details as listed above. Approximately 18 mg of sample was placed into an Al_2O_3 crucible with a pierced lid and heated at $\Delta T/\Delta t = 10$ °C/min in a flowing mixture of CO_2 (Coregas, 99.995 %, 80 mL/min, $p(CO_2) \sim 0.8$ bar) and protective Ar gas (Coregas, 99.995 %, 20 mL/min, $p(Ar) \sim 0.2$ bar) mixture up to 1100 °C. The sample was then held isothermal for 30 min before undergoing consecutive calcination and carbonation steps of 30 min at the same temperature. CO_2 flow (80 mL/min, $p(CO_2) = 0.8$ bar) was employed during carbonation and Ar (20 mL/min) was used for calcination, for a total of 15 cyclic steps.

The cyclic CO_2 absorption/desorption performance of selected samples were further assessed utilising a custom-made Sieverts-type instrument for CO_2 measurements. Details of the instrument and the measurement method can be found in previous studies [15,19,32]. The volumes used were 46.2 cm^3 for the sample side volume, 23.4 cm^3 for the non-ambient volume, and 20.4 cm^3 for the reference volume. Pressure was measured using a Rosemount 3051S pressure transducer (±35 mbar, range 0–140 bar) and temperatures were recorded using a B-type thermocouple (+- 5 °C). An equation of state for CO_2 was used in molar calculations from the NIST Refprop database [33]. Samples (0.6–0.8 g) were loaded into a SiC reactor and heated to 1100 °C ($\Delta T/\Delta t$ = 10 °C/min) by a vertical tube furnace (LABEC VTHTF40/15) under a CO_2 backpressure $p(CO_2) \sim 5$ bar. Samples were held isothermally for 1 h before conducting the first CO_2 desorption step. Desorption was carried out under dynamic vacuum $p(CO_2) \sim 10^{-2}$ bar for 1 h followed by an absorption step under $p(CO_2) \sim 5$ bar for 1 h. These measurements were repeated for 53 absorption-desorption cycles for the sample of $SrCO_3$ – 0.5 M $SrZrO_3$ and 55 cycles for $SrCO_3$ – $SrTiO_3$.

2.4. Sample characterization

Ex-situ Powder X-ray diffraction (XRD) characterisation was performed using a Bruker D8 Advance diffractometer equipped with a Cu $K_{\alpha1,2}$ radiation source and a Lynxeye PSD detector in Bragg-Brentano geometry. Data were collected in the 2θ range from 10° to 80° with a step size of 0.02°. The collected XRD patterns were analysed using Bruker EVA and Bruker TOPAS V.5 software [34].

In-situ synchrotron radiation SR-XRD measurements were conducted at the Powder Diffraction beamline of the Australian Synchrotron, Melbourne, Australia [35]. Data were acquired using a Mythen-II microstrip detector at $\lambda = 0.825040(5)$ Å. Samples were combined with ethanol and smeared onto a prestressed Pt strip within an Anton Paar HTK 2000 strip furnace, a B-type thermocouple (±0.5 %) was attached to the sample., The gas pressure was controlled via a manifold to provide vacuum or 1.5 bar CO_2. The sample was heated from room temperature to 800 °C at $\Delta T/\Delta t$ = 10 °C/min then from 800 °C to 1100 °C at $\Delta T/\Delta t = 10$ at $\Delta T/\Delta t$ = 10–15 °C/min.

The morphological and microstructural structure of samples were characterised using scanning electron microscopy (SEM). The SEM and Energy dispersive X-ray spectroscopy (EDS) data were collected using a Tescan Clara equipped with a secondary electron (SE) detector and an accelerating voltage of 15 kV. Prior to the microscopy analysis, the powder samples were sprinkled onto carbon tape attached to an aluminium stub and were coated with a 20 nm thick layer of conductive carbon.

3. Results and discussion

The successful synthesis of $SrTiO_3$ and $SrZrO_3$ without any detectable side reactions was confirmed using X-ray diffraction (XRD) (see Fig. 1A & Fig. 2A respectively). Furthermore, XRD analysis of the milled samples $SrCO_3$ - 1 M $SrTiO_3$ and $SrCO_3$ - 1 M $SrZrO_3$, demonstrates the absence of any additional unwanted crystalline materials generated during the milling process (Figs. 1B and 2B).

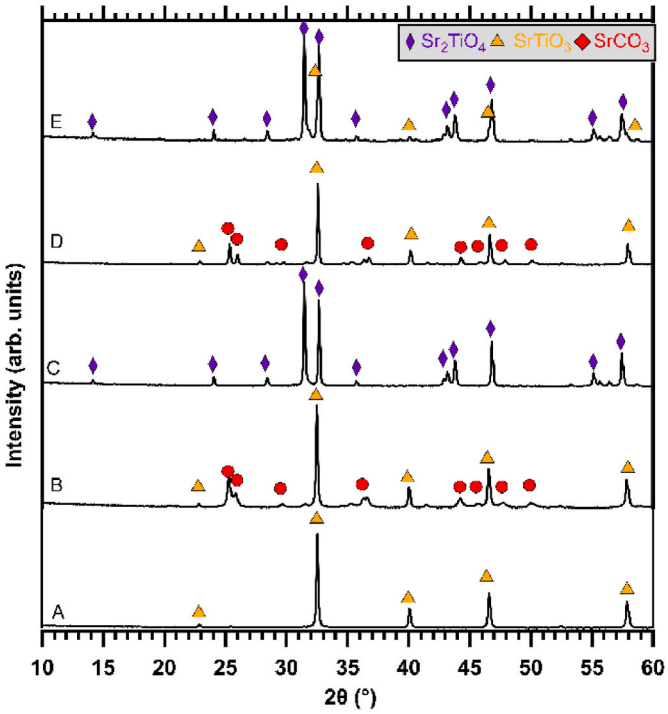

Fig. 1. XRD data (λ = 1.54056 Å) of (A) synthesised $SrTiO_3$; (B) Ball-milled $SrCO_3$ - 1 M $SrTiO_3$; (C) $SrCO_3$ - 1 M $SrTiO_3$ after TGA heating to 1200 °C ($\Delta T/\Delta t$ = 10 °C/min); (D) after 15 CO_2 sorption cycles using TGA at T = 1100 °C for $SrCO_3$ - 1 M $SrTiO_3$, removed after final absorption step; and (E) $SrCO_3$ - 1 M $SrTiO_3$ after Sieverts apparatus measurements for 55 sorption cycles at T = 1100 °C, removed after the final desorption step.

3.1. Thermal behaviour of $SrCO_3$ with $SrTiO_3$ or $SrZrO_3$

From TGA studies (Fig. 3 were), the onset of mass loss (CO_2 release) of both $SrCO_3$ - 1 M $SrTiO_3$ and $SrCO_3$ – 1 M $SrZrO_3$ was detected at a similar temperature compared to pure $SrCO_3$, ~900 °C. It suggests that the addition of $SrTiO_3$ or $SrZrO_3$ does not significantly thermodynamically destabilise the CO_2 release from $SrCO_3$ as additives have in other studies [15,16,18]. A final weight loss of 14.9 % and 12.9 % were observed for $SrCO_3$ – 1 M $SrTiO_3$ and $SrCO_3$ - 1 M $SrZrO_3$ respectively, which are above the theoretical values of 13.29 wt% and 11.75 wt% (determined using the molecular weight of the materials and maximum weight of expected CO_2 release). This suggests the initial wt% loss in the region <100 °C could be due to an amorphous impurity (such as moisture) contained in the composite samples.

After thermal treatment, $SrCO_3$ – 1 M $SrTiO_3$ was removed from the TGA and subjected to XRD analysis, where Sr_2TiO_4 was observed (Fig. 1C). This indicates that $SrTiO_3$ reacts with $SrCO_3$ to form Sr_2TiO_4 as per Eq. (4).

$$SrCO_{3(s)} + SrTiO_{3(s)} \rightarrow Sr_2TiO_{4(s)} + CO_{2(g)} \quad (4)$$

On the other hand, XRD of $SrCO_3$ – 1 M $SrZrO_3$ reveals the presence of two compounds, $SrZrO_3$ and $Sr(OH)_2$ (SrO is known to absorb moisture from the air to form $Sr(OH)_2$) [36]. This suggests that $SrZrO_3$ did not participate as a reactant during CO_2 release and the calcination of $SrCO_3$ occurred via Eq. (5).

$$SrCO_{3(s)} \overset{SrZrO_3}{\rightleftharpoons} SrO_{(s)} + CO_{2(g)} \quad (5)$$

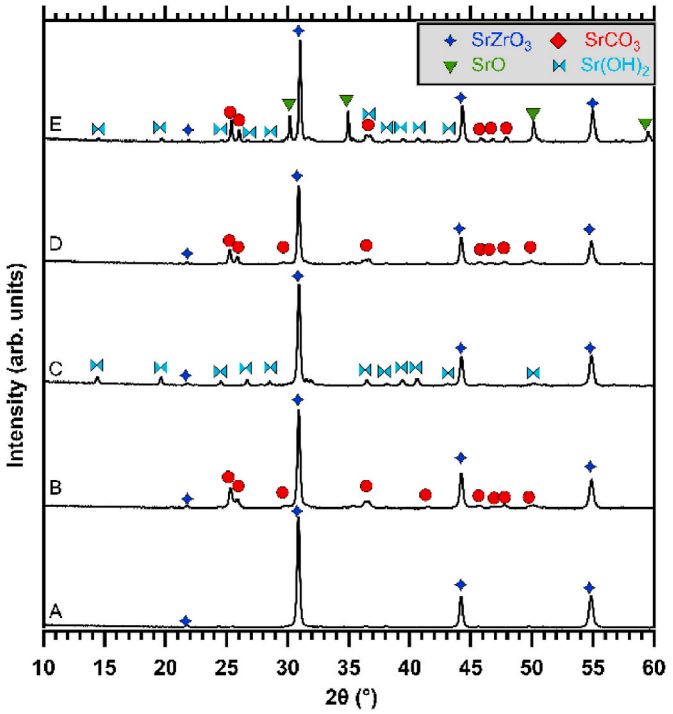

Fig. 2. XRD data (λ = 1.54056 Å) of (A) synthesised $SrZrO_3$; (B) Ball-milled $SrCO_3$ - 1 M $SrZrO_3$; (C) $SrCO_3$ - 1 M $SrZrO_3$ after TGA heating to 1200 °C ($\Delta T/\Delta t$ = 10 °C/min); (D) after 15 CO_2 sorption cycles using TGA at T = 1100 °C for $SrCO_3$ - 1 M $SrZrO_3$, removed after the final absorption step; and (E) $SrCO_3$ - 1 M $SrZrO_3$ after Sieverts apparatus measurements for 53 cycles at T = 1100 °C, removed after the final desorption step. The XRD's for the other ratios are not illustrated as the $SrZrO_3$ is an inert additive and doesn't change the reaction pathway.

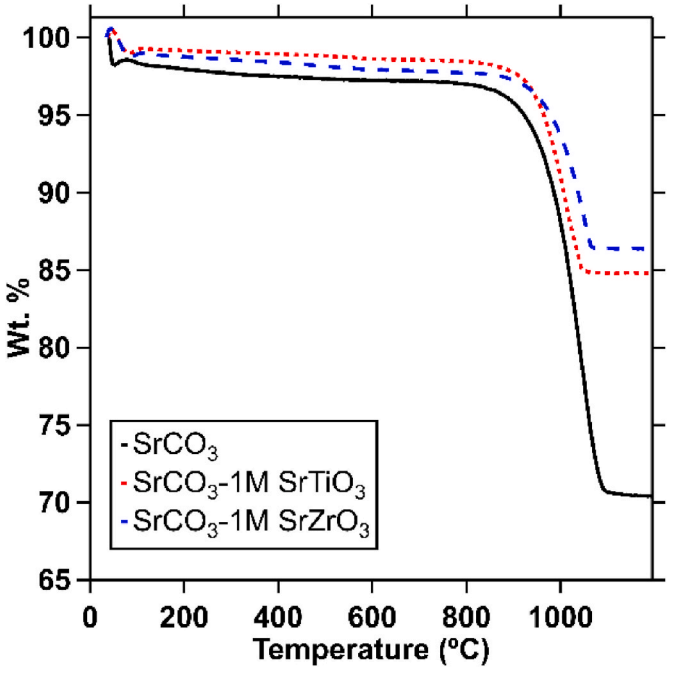

Fig. 3. TGA data comparing the ball-milled (1 h) $SrCO_3$, $SrCO_3$ – 1 M $SrTiO_3$ and $SrCO_3$ – 1 M $SrZrO_3$. Measurement conditions: $\Delta T/\Delta t$ = 10 °C/min, argon flow of 20 mL/min.

3.2. Cyclic stability and calcination/carbonation of the $SrCO_3$ – 1 M $SrTiO_3$ system

The cyclic CO_2 storage stability of two samples, $SrCO_3$ – 1 M $SrTiO_3$ and $SrCO_3$ were evaluated using TGA (Fig. 4). Both samples were heated ($\Delta T/\Delta t$ = 10 °C) up to 1100 °C under a CO_2 atmosphere. They then underwent intermittent calcination and carbonation steps, each lasting for 30 min.

For $SrCO_3$, the initial calcination step resulted in slow CO_2 desorption, accounting for 7.4 wt% compared to the theoretical maximum of 29.8 wt%. Sluggish calcination and carbonation reactions are also observed for $SrCO_3$/SrO after the first cycle, which are indicated by the sloping curves that do not reach completion in the allocated time (30 min). Subsequent sorption cycles decreased in overall CO_2 capacity, stabilising at 3.2 wt% for each absorption step and 3.5 wt% for each desorption step, indicating that CO_2 absorption was slower than desorption, but both were unsatisfactory on this timescale.

In contrast, the $SrCO_3$ – 1 M $SrTiO_3$ composite exhibited an initial CO_2 desorption capacity at the maximum theoretical value of 13.3 wt%. Subsequent CO_2 absorption cycles showed a rapid reabsorption of the desorbed CO_2, and over 15 cycles, a slight weight gain of approximately 1 wt% was observed. This slight increase in weight suggests the presence of a minor amount of amorphous SrO in the initial composite, which is undetectable by XRD, possibly from trace hydroxide decomposed from the starting material during the initial thermal treatment. This oxide subsequently converts to $SrCO_3$ during reaction with CO_2. The cyclic CO_2 capacity stabilises at 11.5 wt% (85 % of the theoretical maximum).

After the final CO_2 absorption cycle, the sample was cooled and XRD was performed, where $SrTiO_3$ and $SrCO_3$ were observed (Fig. 1D). This demonstrates that the sample reforms $SrCO_3$ and $SrTiO_3$ after multiple CO_2 cycles and thus Eqn. (4) is reversible. The incorporation of $SrTiO_3$ into $SrCO_3$ resulted in a significant enhancement in the cyclic capacity and stability of the composite compared to pristine $SrCO_3$.

The cyclic stability of $SrCO_3$ - 1 M $SrTiO_3$ was further assessed using CO_2 absorption measurements conducted with a Sieverts type apparatus (Fig. 5). This employed a larger sample size of 0.81 g (compared to mg-scale in the TGA) and higher CO_2 absorption pressures ($p(CO_2)$ ~ 5 bar) along with longer sorption times (1 h absorption and 1 h desorption steps), aiming to better represent the thermodynamic and cyclic stability/energy capacity under conditions relevant to potential industrial operations [4].

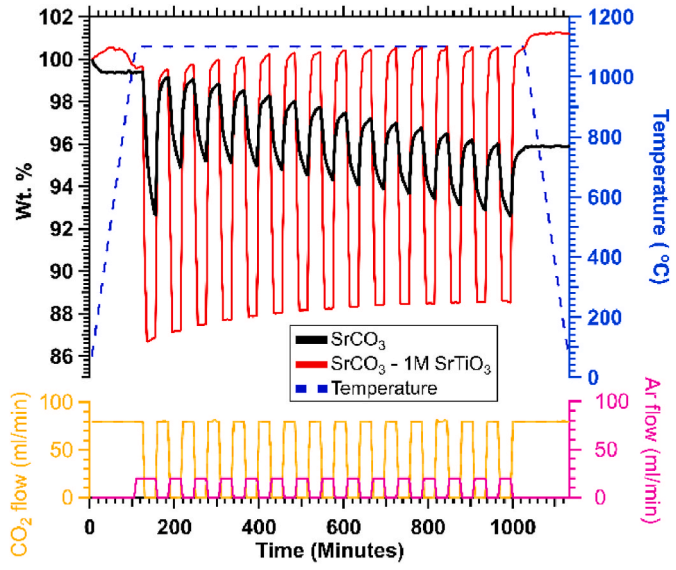

Fig. 4. TGA cycling measurements of $SrCO_3$ and $SrCO_3$ - 1 M $SrTiO_3$ over 15 CO_2 desorption and absorption cycles at 1100 °C.

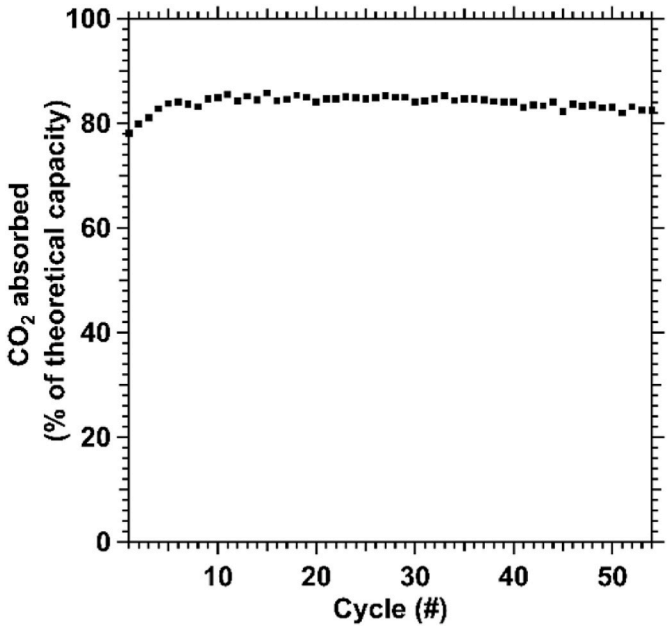

Fig. 5. CO_2 storage capacity of $SrCO_3$ – 1 M $SrTiO_3$ over 55 cycles. Measurements were carried out using Sieverts method at 1100 °C, mass = 0.81 g, abs/desorption $p(CO_2)$ = (5 bar/0 bar), t = (1 h/1 h).

The $SrCO_3$ - 1 M $SrTiO_3$ composite consistently maintains a stable CO_2 capacity at approximately 85 % of the theoretical maximum throughout 55 cycles, which aligns well with the TGA results on a smaller scale (see Fig. 4). An initial increase in cyclic capacity is observed over the initial five cycles and this likely due to the amorphous SrO content in the sample which is activated and carbonated during these cycles. A slight decline in capacity (~2 % of the theoretical maximum) is observed over the 55 cycles, which can be attributed to morphological changes that will be discussed in detail below. After the final CO_2 desorption cycle, XRD analysis was conducted to confirm the reaction products, namely Sr_2TiO_4 and a minor trace of $SrTiO_3$ (Fig. 1E), which confirms the validity of Eqn. (4). These findings highlight the excellent CO_2 cyclic capacity and stability exhibited by $SrCO_3$ - 1 M $SrTiO_3$ on a larger scale with elevated CO_2 pressures.

In-situ SR-XRD data was collected on ~0.2 g of $SrCO_3$ - 1 M $SrTiO_3$ heated to 1100 °C under a CO_2 atmosphere ($p(CO_2)$ = 1.5 bar) (Fig. 6). At 931 °C, $SrCO_3$ undergoes a polymorphic phase transition from (orthorhombic) α to (hexagonal) β phase, as expected to occur in the temperature range of 925–933 °C [37]. The sample reached 1100 °C without showing evidence of decomposition, this is expected due to the partial pressure of CO_2 being above the expected equilibrium partial pressure ($p(CO_2$ = 0.62 bar). The CO_2 release reaction was initiated by the application of vacuum ($p(CO_2)$ ~ 0 bar) at 1100 °C, where the reaction of β-$SrCO_3$ and $SrTiO_3$ to form Sr_2TiO_4 was observed. The results support the *ex-situ* XRD data revealing Sr_2TiO_4 is the final solid product from the decomposition of the $SrCO_3$ - 1 M $SrTiO_3$ composite. On re-application of CO_2 pressure ($p(CO_2)$ = 1.5 bar) the Bragg peaks of Sr_2TiO_4 disappear completely and β-$SrCO_3$ and $SrTiO_3$ reform.

Additionally, it is interesting to note that a minor amount of a metastable $Sr_3Ti_2O_7$ intermediate is formed during the calcination. The reason that $Sr_3Ti_2O_7$ is not observed from *ex-situ* XRD data could be due to its lower thermal stability than Sr_2TiO_4 [38]. As such, the formed $Sr_3Ti_2O_7$ intermediate may revert to Sr_2TiO_4 on cooling. The formation of a $Sr_3Ti_2O_7$ intermediate could contribute greatly to the superior long-term CO_2 cyclic stability of $SrCO_3$–$SrTiO_3$ systems because it may act as a grain-growth inhibitor to prevent sintering. The addition of unreactive oxides to TCES materials has previously been shown to inhibit sintering [39].

To investigate the morphological changes occurring during cyclic CO_2 absorption and desorption at high temperature, both milled and cycled samples of $SrCO_3$ - 1 M $SrTiO_3$ were analysed using SEM-EDS (Fig. 7). The milled sample consists of small particles (~100 nm) and exhibits an even distribution of Ti and Sr distributed homogenously throughout the composite, indicating a well-mixed sample (Fig. 7a). Both the TGA cycled (Fig. 7b) and Sieverts cycled (Fig. 7c) samples exhibit larger particles (~1 μm) that appear sintered together. This has been observed in pure $SrCO_3$ and many other metal carbonate and hydride materials and has often been cited for the poor cyclic performance of materials [16,19,37]. The sintering process leads to a reduction in the surface area and porosity of the sample, which is expected given the high operating temperature during cycling. Consequently, the diffusion of CO_2 into the sample may slow down with each additional cycle if particle growth becomes excessive. However, there is evidence of channels within larger agglomerates, which could facilitate CO_2 flow, aligning with the observed high reactivity towards CO_2. Furthermore, the

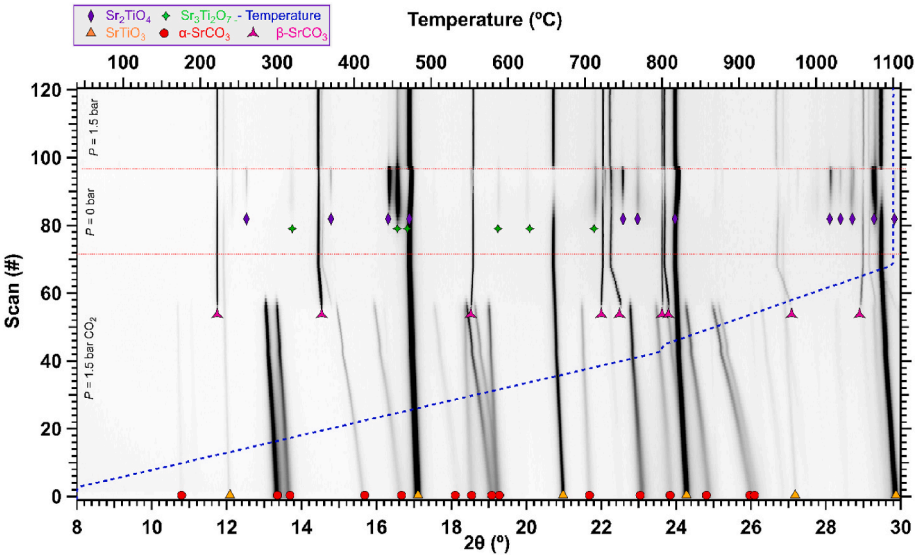

Fig. 6. *In-situ* SR-XRD data of $SrCO_3$ – 1 M $SrTiO_3$ heated from room temperature to 1100 °C ($\Delta T/\Delta t$ = 10–15 °C/min; λ = 0.825040(5) Å, $p(CO_2)$ = 0 or 1.5 bar). The blue dashed line represents the temperature profile. (For interpretation of the references to colour in this figure legend, the reader is referred to the Web version of this article.)

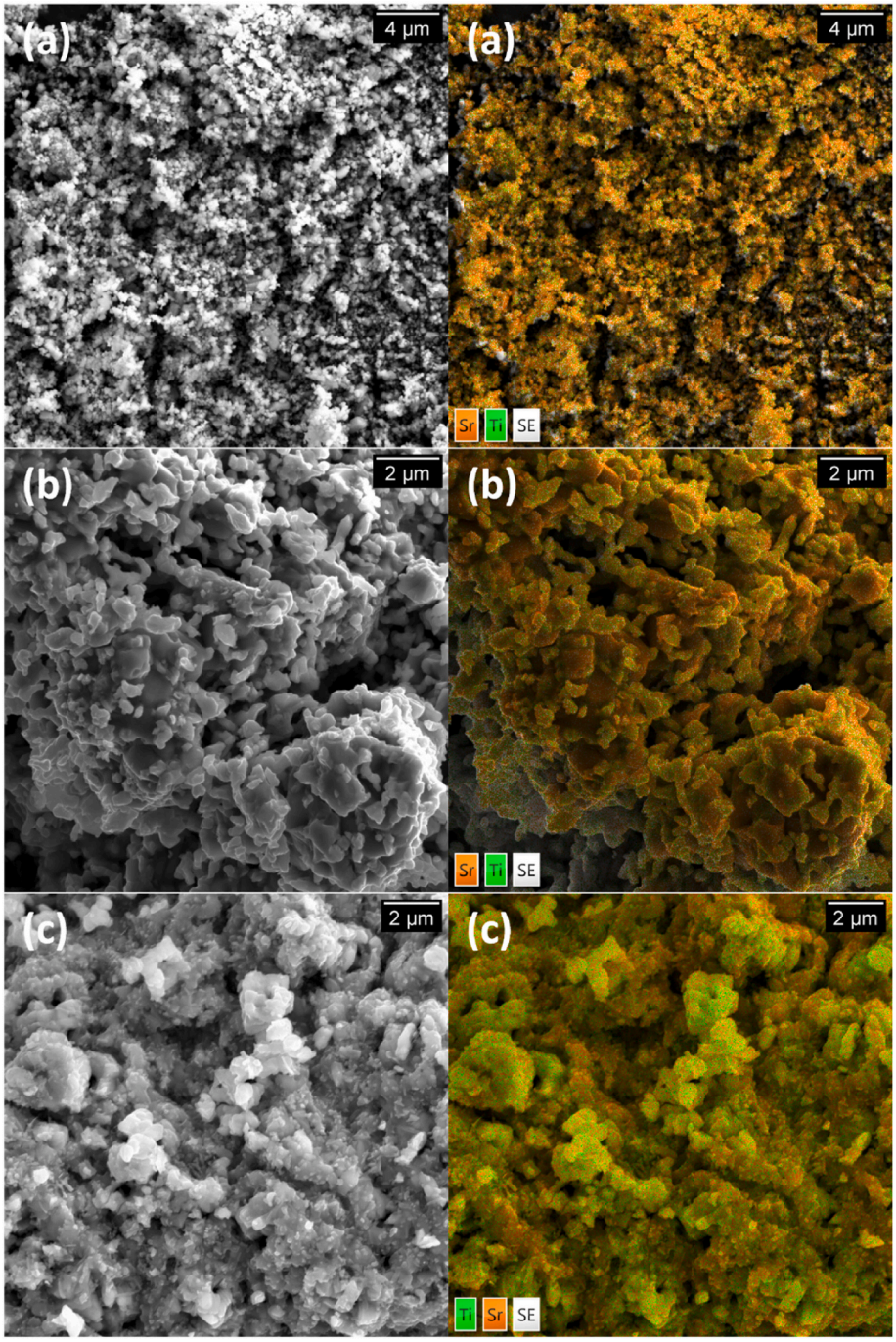

Fig. 7. SEM (left) and EDS (right) mapping of $SrCO_3$ - 1 M $SrTiO_3$ in SE mode, 15 kV: (a) Ball-milled; (b) after 15 cycles at 1100 °C, TGA, removed after CO_2 absorption; and (c) after 55 cycles at 1100 °C, Sieverts apparatus, removed after CO_2 desorption. Colour code: Sr (Orange); Ti (green). (For interpretation of the references to colour in this figure legend, the reader is referred to the Web version of this article.)

distribution of Ti and Sr remains uniform in both cycled samples throughout, indicating no obvious phase segregation that could limit reactivity. Under the test conditions in this study, the $SrCO_3$ - 1 M $SrTiO_3$ composite maintains a stable cycling capacity of ~80 % in both TGA and Sieverts experiments (see Figs. 4 and 5) despite the observed grain growth and sintering. This could be attributed to the previously mentioned formation of the intermediate $Sr_3Ti_2O_7$ (see Fig. 6) and the lack of particles or agglomerates larger than micron-scale.

3.3. Cyclic stability and calcination/carbonation of the $SrCO_3$–$SrZrO_3$ system

TGA was utilised to compare the mass change profiles between $SrCO_3$ and the $SrCO_3$ - 1 M $SrZrO_3$ system during 15 CO_2 sorption cycles (see Fig. 8). The $SrCO_3$ - 1 M $SrZrO_3$ composite demonstrates exceptional stability in its CO_2 cycling capacity over 15 cycles. Furthermore, the inclusion of $SrZrO_3$ significantly enhances the CO_2 absorption kinetics, as indicated by the steep curves during the carbonation step. In each cycle, the carbonation process occurs rapidly and reaches its maximum theoretical value (11.8 wt%). In contrast, $SrCO_3$ exhibits sluggish kinetics and a diminished cyclic capacity, as discussed earlier (see section

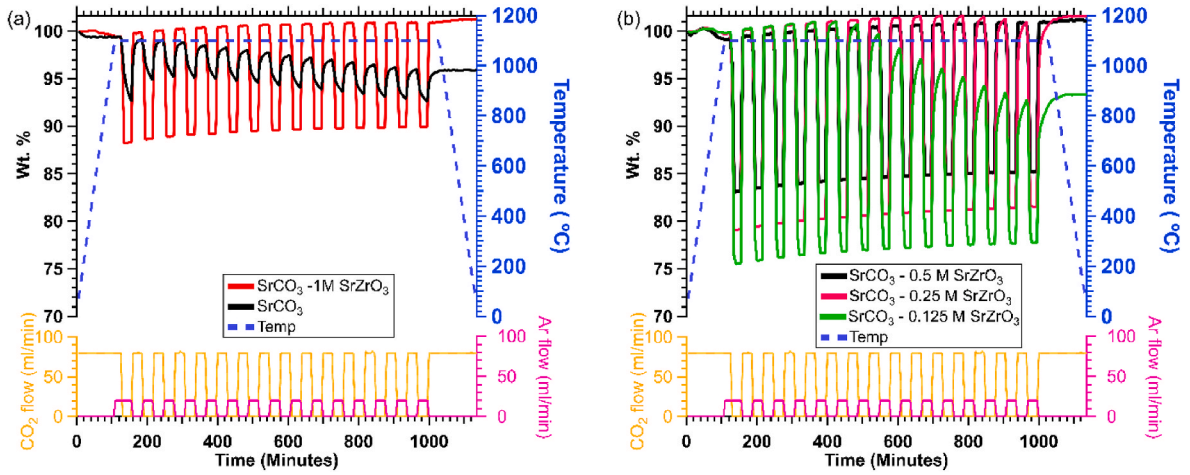

Fig. 8. TGA measured mass change of (a) $SrCO_3$ – black; $SrCO_3$ – 1 M $SrZrO_3$-blue. (b) $SrCO_3$ – 0.5 M $SrZrO_3$ - purple; $SrCO_3$ – 0.25 M $SrZrO_3$ - teal; $SrCO_3$ – 0.125 M $SrZrO_3$ – green, 15 CO_2 desorption and absorption cycles at 1100 °C. (For interpretation of the references to colour in this figure legend, the reader is referred to the Web version of this article.)

2.3).

It was found in section 3.1 that the $SrZrO_3$ additive does not participate in a thermochemical reaction with $SrCO_3$ but acts as an inert additive and possible sintering inhibitor. It is beneficial to optimise the content of an inert additive to achieve high energy density and low cost without sacrificing cyclic stability. The effect of the $SrZrO_3$ additive content on the multicycle performance of $SrCO_3$ was further studied using TGA. Fig. 8b shows the weight change of $SrCO_3$ with various additive content of $SrZrO_3$ during 15 CO_2 desorption and absorption cycles at 1100 °C. The samples with 1 M and 0.5 M $SrZrO_3$ loading maintain stable capacity throughout the 15 cycles. Whilst the capacity drops gradually after 10 and 5 cycles for the samples with 0.25 M and 0.125 M loading of $SrZrO_3$, respectively. The carbonation rate also decreases with increasing number of cycles in these samples, this is particularly obvious for the $SrCO_3$-0.125 M $SrZrO_3$ sample. Comparing similar samples with differing $SrZrO_3$ content demonstrates that cycling stability decreases as the $SrCO_3$ content exceeds at least 62 % by mass (with 0.25 M $SrZrO_3$ loading). A low ratio of $SrZrO_3$ loading is unable to maintain high CO_2 cyclic capacity.

It is important to note that the TGA results herein demonstrate a much higher CO_2 capacity than those of Rhodes et al. [27]. One possible reason is the selected temperature of 1235 °C for carbonation in the previous study is too high for SrO to absorb CO_2, where according to thermodynamics the equilibrium pressure of the carbonation of SrO is expected to be 1.25 bar, which is higher than the applied pressure of their measurements (0.9 bar) [27,40].

Given that $SrCO_3$-0.5 M $SrZrO_3$ (44 wt% $SrZrO_3$) demonstrated excellent cycling stability over 15 cycles in TGA analysis, while maintaining a higher energy density compared to $SrCO_3$-1M $SrZrO_3$ (60 wt% $SrZrO_3$), it was selected for further investigation using the Sieverts apparatus to evaluate its extended capacity. Fig. 9 showsshows the CO_2 absorption capacity of $SrCO_3$-0.5 M $SrZrO_3$ over 53 cycles.

Interestingly, unlike the results obtained from TGA measurements, the CO_2 absorption capacity declines from 86 % during the first cycle to 11 % after 53 cycles. The Sieverts measurement provides a more realistic analysis than TGA, as it employs a larger sample size of 0.8 g compared to the small amount (15–20 mg) used in TGA measurements. This highlights the inefficiency of testing TCES materials using only TGA as factors such as heat transfer and bulk morphological properties may influence the cyclic capacity [10]. For instance, poor thermal conductivity could result in thermal spikes during CO_2 absorption that could lead to further sintering and degradation of the material.

The observed decrease in capacity implies that the 0.5 M $SrZrO_3$ ratio may not be sufficient to overcome the decline in multicycle activity

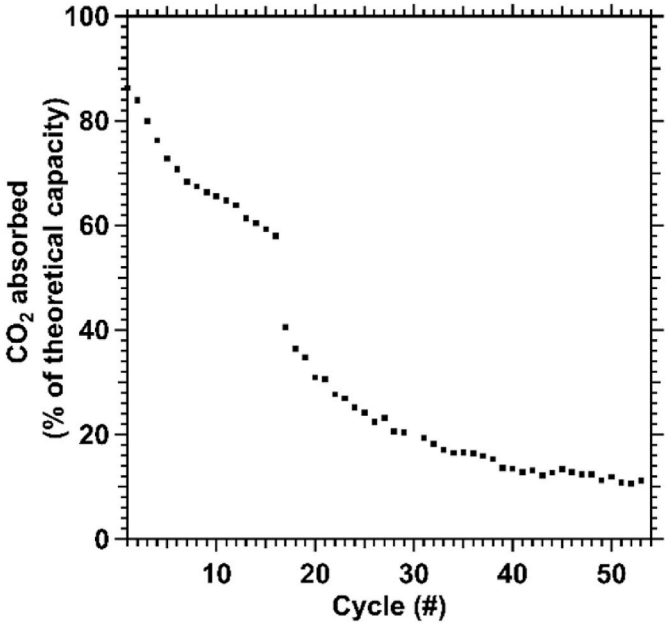

Fig. 9. CO_2 storage capacity of $SrCO_3$ – 0.5 M $SrZrO_3$ over 53 cycles. Measurements were carried out using the Sieverts method at 1100 °C.

resulted from sintering. Specifically, there is a significant drop from 58 % to 41 % in CO_2 capacity after 16 cycles, which could be attributed to the rapid growth of particles caused by thermal annealing, leading to a significant reduction in porosity.

The particle morphology of the as-milled and CO_2 cycled $SrCO_3$ - 0.5 M $SrZrO_3$ samples is shown in Fig. 10. The milled composite consists of finely mixed small particles <1 μm (Fig. 10a) and Sr and Zr are homogeneously dispersed throughout the sample. After the sample is subjected to 15 cycles in the TGA at 1100 °C (Fig. 10b), Sr is concentrated in areas in which the SEM image shows a flat plate-like agglomerate. The large (10's μm) agglomerate results from the substantial sintering of aggregated $SrCO_3$/SrO particles. On the other hand, some Zr is spread away from the $SrCO_3$/SrO clusters, showing some phase segregation. Cycling in Sieverts apparatus causes the $SrCO_3$/SrO to show more substantial sintering (100's μm) while $SrZrO_3$ regions appear separate with some particles possibly trapped in the agglomerated $SrCO_3$ (Fig. 10C).

It is clear that $SrCO_3$ - 0.5 M $SrZrO_3$ has a radically different

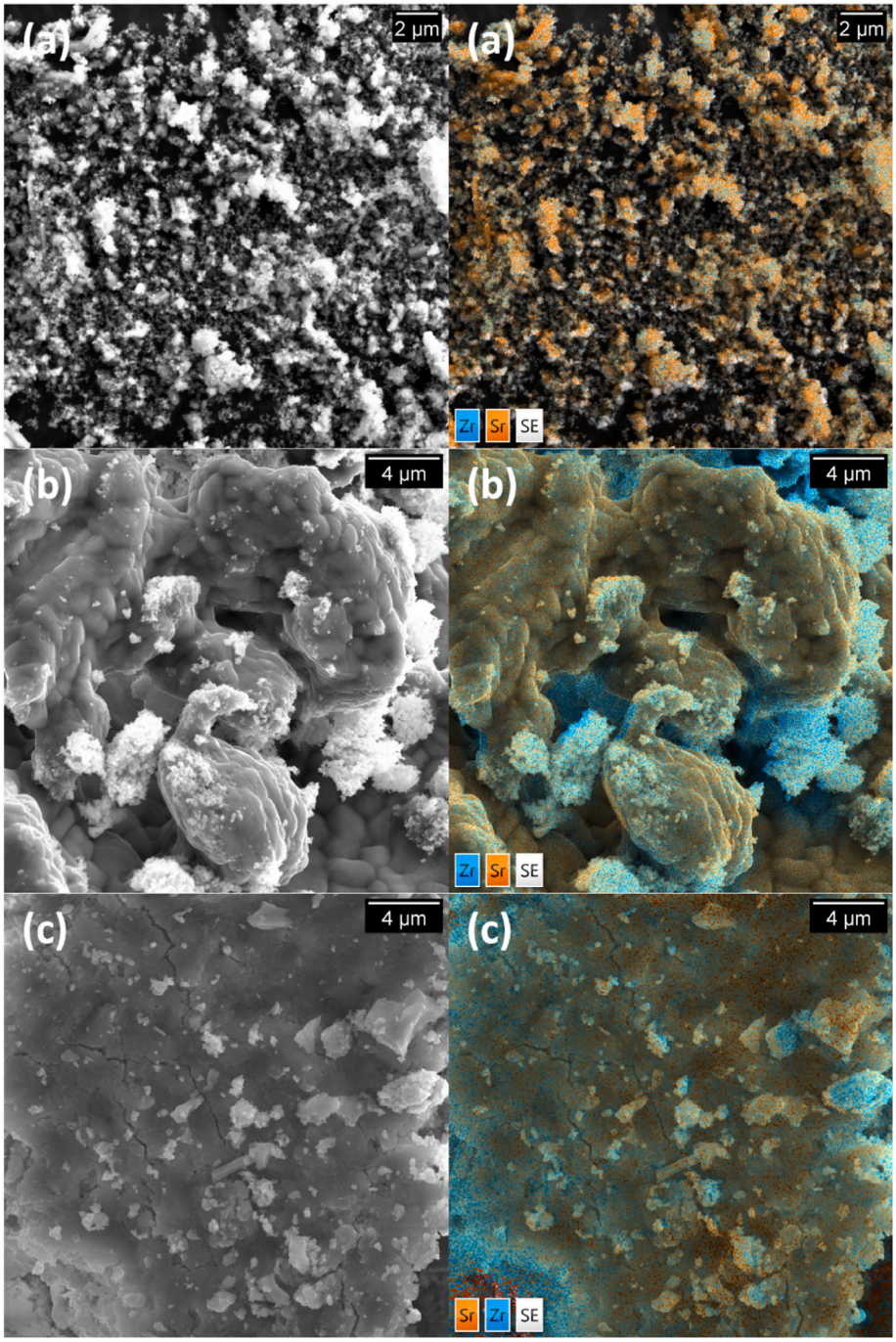

Fig. 10. SEM (left) and EDS (right) mapping of $SrCO_3$ - 0.5 M $SrZrO_3$ at 15 kV: (a) as ball-milled; (b) after 15 cycles at 1100 °C, TGA, removed after CO_2 absorption; (c) after 52 cycles at 1100 °C in the Sieverts apparatus, removed after CO_2 desorption. Colour code: Sr (Orange); Zr (blue). (For interpretation of the references to colour in this figure legend, the reader is referred to the Web version of this article.)

morphology to $SrCO_3$-1M $SrTiO_3$, which may result in the different cycling performance observed between these two composite systems. Large SrO particles may hinder CO_2 uptake and could limit the cyclic capacity of the $SrCO_3$ - 0.5 M $SrZrO_3$ system in TGA and/or Sieverts studies. The large cyclic capacity drop observed in Sieverts measurements indicates that particles larger than 10's of micron in size could be the limit for satisfactory kinetics. In the case of large particles, only part of the SrO reacts with CO_2 to form $SrCO_3$ on the external surface of unreacted SrO [27,41,42]. The $SrCO_3$ external shell formed could in-turn block access of CO_2 to the inner SrO particles. An additional factor affecting the disparity in the cyclic performance could be caused by the differences in thermal conductivity of the additives. $SrTiO_3$ has a higher thermal conductivity of ~6–12 W/m·K at 1100 °C compared to ~2.3 W/m·K for $SrZrO_3$ at 1100 °C [43,44]. The effect of this sintering may scale with sample size (due to heat dissipation) and may not be as apparent in TGA samples where heat flow and sintering do not play such a large role.

4. Cost analysis

For these metal carbonates to be feasible as TCES materials, they must not only be physically optimised to reversibly store CO_2, and operate at the required gas pressure and temperature, they must also be economically feasible. Ultimately, this means that they must be cheaper

Table 2
Comparison of thermochemical properties, system variables, and cost parameters for select energy storage materials to store 1 TJ of electrical energy [16,18,45,46].

	$SrCO_3 \rightleftharpoons SrO + CO_2$	$SrCO_3 + SrTiO_3 \rightleftharpoons Sr_2TiO_4 + CO_2$	$SrCO_3 + 0.5SrZrO_3 \rightleftharpoons 0.5SrZrO_3 + SrO + CO_2$	$SrCO_3 + SrSiO_3 \rightleftharpoons Sr_2SiO_4 + CO_2$	Molten salt ($40NaNO_3$:$60KNO_3$)
Enthalpy ΔH (kJ mol^{-1} of CO_2)	201.39	176	206	155.7	–
Molar Mass (g mol^{-1}) (CO_2 loaded)	147.6	331	261	311	94.6
Density (g cm^{-3})[a]	3.5	4.2	4.2	3.75[b]	2.17
CO_2 Capacity (wt.%)	29.8	13.3	16.9	14.1	–
Gravimetric Energy Density (kJ kg^{-1})	1364	531	788	500	413
Volumetric Energy Density (MJ m^{-3})[a]	1326	2242	3303	1878	895
Operating Temperature (°C)	1220	1100	1100	700	290–565
Operating CO_2 Pressure (bar)	0–1	0–5	0–5	0.1–6	–
Theoretical Carnot Efficiency (%)	79.7	77.9	77.9	69	46
Estimated Practical Efficiency (%)	55	53	53	45	27
Mass Required (tonnes)	1334	3554	2392	4700	9100
Volume Required (m^3)	381	841	570	1711	4194
Materials Cost (US$/tonne)[c]	1060	1372[d]	1301[d]	480	630
Energy Cost (US$/kWh)	2.79	17.55	11.20	8.13	5.8
Total Materials Cost Required (US$)	1,414,066	4,876,012	3,112,376	2,258,099	5,730,000

[a] Intrinsic crystalline density used to calculate volumetric density.
[b] 80 wt% $SrSiO_3$:$SrCO_3$ + 20 wt% NaCl:$MgCl_2$.
[c] Costs derived from references in Table header.
[d] Cost based on the price of the corresponding oxide, TiO_2 and ZrO_2.
[e] Total cost of materials to store 1 TJ of electricity. Assuming 100 % cycling capacity.

to integrate than the current state-of-art materials which are molten salts. A physical and economic comparison between molten salts, the TCES materials studied in this manuscript and a selection of other $SrCO_3$ based TCES materials has been made and is presented in Table 2. As can be seen, the cost of pure $SrCO_3$ makes it the most cost-effective option at 2.79 US$/kWh, but the poor cyclic activity counteracts this assessment. Although the strontium zirconate and titanate additives are competitive from a US$/kWh perspective (9.94 and 17.73 US$/kWh, respectively) they are outperformed by the strontium silicate additive (8.13 US $/kWh). They do however have higher volumetric and gravimetric densities and produce more energy per mole of CO_2 so will require less CO_2 gas storage volume. The zirconate additive has the edge in every category over the titanate additive due to its higher percentage of $SrCO_3$, but unless a method to mitigate the cyclic capacity loss of this material is implemented the titanate will perform better over multiple cycles. This cost analysis is reliable only on a pure material-based comparison, and therefore, additional costs and a complete techno-economic assessment is recommended in future studies [4].

In comparison to other TCES materials that have shown promise, the materials presented in this study are beneficial due to their high operating temperature, which aligns with the operating temperatures of CSP plants and heat engines. As far as cost is concerned, they are comparable to metal hydride TCES materials with the $CaH_2 + 2Al$ system costing 9.2 US$/$kWh_{th}$ (operating at a maximum of 500 °C at 1 bar H_2) and the $SrH_2 + 2Al$ system costing 17.1 US$/$kWh_{th}$ (operating at a maximum of 846 °C at 1 bar H_2) [12]. There are cheaper metal hydride TCES materials such as Mg_2FeH_6 but these have a much lower operating temperature that aren't feasible for CSP applications [47]. To date, the most cost effective TCES material that operates at ~900 °C stands to be the $CaCO_3$ system that costs ~10 US$/tonne [19] compared to the lowest in this study of 480 US$/tonne [18] for the $SrCO_3$ + $SrSiO_3$ system, although costs would be expected to diminish with increased rates of production.

5. Conclusions

It is clear that thermal energy storage is posed to provide heat storage for a range of applications and conditions. The comparison between $SrZrO_3$ and $SrTiO_3$ as additives to $SrCO_3$ highlights their contrasting characteristics. Notably, $SrTiO_3$ exhibits inherent resistance to cyclic CO_2 capacity decline on both smaller scale TGA experiments and larger scale experiments using Sieverts apparatus (maintaining over 80 % capacity), indicating its potential suitability for upscaling. Whilst the use of $SrZrO_3$ as an additive offers lower material costs relative to $SrTiO_3$ (9.94–17.73 US$/kWh), it fails to prevent sintering and enhance CO_2 cyclic capacity on a larger scale. The contrast in performance may be due to the ability of $SrTiO_3$ to actively take part in the reaction pathway with $SrCO_3$, whereas $SrZrO_3$ acts as an inert additive and is unable to completely prevent sintering at 1100 °C.

This study emphasizes the significance of studying materials under diverse conditions, as expecting consistent performance from mg-scale TGA to large-scale systems can be unrealistic. Future recommendations involve the exploration of cost-effective additives that undergo morphological changes near the operating temperature of the active metal carbonate, aiming to disrupt the sintering process and improve capacity. Additionally, conducting further studies on TCES materials in larger-scale systems, where bulk effects are more pronounced, would be valuable. Additionally, Sieverts apparatus could be used as an effective steppingstone to test TCES materials on a scale between TGA and benchtop scale prototypes.

CRediT authorship contribution statement

Kyran Williamson: Writing – review & editing, Writing – original draft, Methodology, Investigation, Formal analysis, Data curation, Conceptualization. **Yurong Liu:** Writing – review & editing, Writing –

original draft, Methodology, Investigation, Formal analysis, Data curation, Conceptualization. **Terry D. Humphries:** Writing – review & editing, Writing – original draft, Supervision, Project administration, Methodology, Investigation, Funding acquisition, Formal analysis, Data curation, Conceptualization. **Anita M. D'Angelo:** Writing – review & editing, Writing – original draft, Investigation, Formal analysis, Data curation. **Mark Paskevicius:** Writing – review & editing, Writing – original draft, Supervision, Project administration, Methodology, Investigation, Funding acquisition, Formal analysis, Data curation, Conceptualization. **Craig E. Buckley:** Writing – review & editing, Writing – original draft, Supervision, Project administration, Funding acquisition, Conceptualization.

Declaration of competing interest

The authors declare the following financial interests/personal relationships which may be considered as potential competing interests: Mark Paskevicius reports financial support was provided by Department of Industry Innovation and Science. Mark Paskevicius reports financial support was provided by Australian Research Council. Kyran Williamson reports financial support was provided by Commonwealth of Australia. Kyran Williamson reports financial support was provided by AINSE Ltd.

Data availability

Data will be made available on request.

Acknowledgements

CEB, MP and TDH acknowledge the Global Innovation Linkage project for grant GIL73589. CEB, MP, TDH acknowledge the Australian Research Council for ARC Discovery project grant DP200102301. KW acknowledges the Australian Government for an Australian Government Research Training Program Scholarship. This research was supported by an AINSE Ltd through a Postgraduate Research Award (PGRA) for KW. SEM and XRD research were undertaken using the Tescan Mira3 EM (ARC LE130100053) and the Bruker D8 Advance XRD instrumentation (ARC LE0775551) at the John de Laeter Centre, Curtin University. ANSTO is acknowledged for providing access to the PD beamline at the Australian Synchrotron, Melbourne, Australia.

References

[1] IRENA. I. *Global energy Transformation: a Roadmap to 2050*. 2019 Edition 2019 2019. https://www.irena.org/publications/2019/Apr/Global-energy-transformation-A-roadmap-to-2050-2019Edition.
[2] Forrester J. The value of CSP with thermal energy storage in providing Grid stability. Energy Proc 2014;49:1632–41. https://doi.org/10.1016/j.egypro.2014.03.172.
[3] Sarbu I, Sebarchievici C. A Comprehensive review of thermal energy storage. Sustainability 2018;10(1):191. https://doi.org/10.3390/su10010191.
[4] Bayon A, Bader R, Jafarian M, Fedunik-Hofman L, Sun Y, Hinkley J, Miller S, Lipiński W. Techno-economic assessment of solid–gas thermochemical energy storage systems for solar thermal power applications. Energy 2018;149:473–84. https://doi.org/10.1016/j.energy.2017.11.084.
[5] Copus M, Fraser B, Reece R, Hands S, Cuskelly D, Sugo H, Reed S, Bradley J, Post A, Kisi E. On-sun testing of miscibility gap alloy thermal storage. Sol Energy 2019;177:657–64. https://doi.org/10.1016/j.solener.2018.11.048.
[6] Steinmann W-D. Thermal energy storage for medium and high temperatures: Concepts and applications. Wiesbaden: Springer Fachmedien Wiesbaden; 2022. https://doi.org/10.1007/978-3-658-02004-0.
[7] Bayon A, Carrillo AJ, Mastronardo E, Coronado JM. Chapter six - thermochemical heat storage at high temperature. In: Lipiński W, editor. Advances in Chemical Engineering. Solar Thermochemistry, vol. 58. Academic Press; 2021. p. 247–95. https://doi.org/10.1016/bs.ache.2021.10.004.
[8] Pardo P, Deydier A, Anxionnaz-Minvielle Z, Rougé S, Cabassud M, Cognet P. A review on high temperature thermochemical heat energy storage. Renew Sustain Energy Rev 2014;32:591–610. https://doi.org/10.1016/j.rser.2013.12.014.
[9] André L, Abanades S. Recent advances in thermochemical energy storage via solid–gas reversible reactions at high temperature. Energies 2020;13(22):5859. https://doi.org/10.3390/en13225859.
[10] Desage L, McCabe E, Vieira AP, Humphries TD, Paskevicius M, Buckley CE. Thermochemical batteries using metal carbonates: a review of heat storage and extraction. J Energy Storage 2023;71:107901. https://doi.org/10.1016/j.est.2023.107901.
[11] Harries DN, Paskevicius M, Sheppard DA, Price TEC, Buckley CE. Concentrating solar thermal heat storage using metal hydrides. Proc IEEE 2012;100(2):539–49. https://doi.org/10.1109/JPROC.2011.2158509.
[12] Humphries TD, Paskevicius M, Alamri A, Buckley CE. Thermodynamic Destablization of SrH_2 using Al for the next generation of high temperature thermal batteries. J Alloys Compd 2022;894:162404. https://doi.org/10.1016/j.jallcom.2021.162404.
[13] Poupin L, Humphries TD, Paskevicius M, Buckley CE. A thermal energy storage prototype using sodium magnesium hydride. Sustain Energy Fuels 2019;3(4):985–95. https://doi.org/10.1039/C8SE00596F.
[14] Poupin L, Humphries TD, Paskevicius M, Buckley CE. An experimental high temperature thermal battery coupled to a low temperature metal hydride for solar thermal energy storage. Sustain Energy Fuels 2020;4(1):285–92. https://doi.org/10.1039/C9SE00538B.
[15] Møller KT, Williamson K, Buckley CE, Paskevicius M. Thermochemical energy storage properties of a barium based reactive carbonate composite. J Mater Chem A 2020;8(21):10935–42. https://doi.org/10.1039/D0TA03671D.
[16] Humphries TD, Møller KT, Rickard WDA, Sofianos MV, Liu S, Buckley CE, Paskevicius M. Dolomite: a low cost thermochemical energy storage material. J Mater Chem A 2019;7(3):1206–15. https://doi.org/10.1039/C8TA07254J.
[17] Møller KT, Humphries TD, Berger A, Paskevicius M, Buckley CE. Thermochemical energy storage system development utilising limestone. Chemical Engineering Journal Advances 2021;8:100168. https://doi.org/10.1016/j.ceja.2021.100168.
[18] Pires Vieira A, Williamson K, Humphries T, Paskevicius M, Buckley C. A new strontium based reactive carbonate composite for thermochemical energy storage. J Mater Chem A 2021;9. https://doi.org/10.1039/D1TA04363C.
[19] Møller KT, Ibrahim A, Buckley CE, Paskevicius M. Inexpensive thermochemical energy storage utilising additive enhanced limestone. J Mater Chem A 2020;8(19):9646–53. https://doi.org/10.1039/D0TA03080E.
[20] Desage L, Humphries TD, Paskevicius M, Buckley CE. Calcium hydride with aluminium for thermochemical energy storage applications. Sustain Energy Fuels 2023;8(1):142–9. https://doi.org/10.1039/D3SE01122D.
[21] Amghar N, Ortiz C, Perejón A, Valverde JM, Maqueda LP, Sánchez Jiménez PE. The $SrCO_3$/SrO system for thermochemical energy storage at ultra-high temperature. Sol Energy Mater Sol Cell 2022;238:111632. https://doi.org/10.1016/j.solmat.2022.111632.
[22] Fedunik-Hofman L, Bayon A, Donne S. Calcium, strontium and barium carbonate mixtures for calcination-carbonation thermochemical energy storage. AIP Conf Proc 2019;2126(1):210002. https://doi.org/10.1063/1.5117751.
[23] Khosa AA, Zhao CY. Heat storage and release performance analysis of $CaCO_3$/CaO thermal energy storage system after Doping Nano Silica. Sol Energy 2019;188:619–30. https://doi.org/10.1016/j.solener.2019.06.048.
[24] Zhao M, Shi J, Zhong X, Tian S, Blamey J, Jiang J, Fennell PS. A Novel Calcium Looping absorbent incorporated with polymorphic Spacers for Hydrogen production and CO_2 capture. Energy Environ Sci 2014;7(10):3291–5. https://doi.org/10.1039/C4EE01281J.
[25] Mostafavi E, Sedghkerdar MH, Mahinpey N. Thermodynamic and kinetic study of CO_2 capture with Calcium based Sorbents: experiments and Modeling. Ind Eng Chem Res 2013;52(13):4725–33. https://doi.org/10.1021/ie400297s.
[26] Bagherisereshki E, Tran J, Lei F, AuYeung N. Investigation into SrO/$SrCO_3$ for high temperature thermochemical energy storage. Sol Energy 2018;160:85–93. https://doi.org/10.1016/j.solener.2017.11.073.
[27] Rhodes NR, Barde A, Randhir K, Li L, Hahn DW, Mei R, Klausner JF, AuYeung N. Solar thermochemical energy storage through carbonation cycles of $SrCO_3$/SrO supported on $SrZrO_3$. ChemSusChem 2015;8(22):3793–8. https://doi.org/10.1002/cssc.201501023.
[28] Maya JC, Chejne F, Gómez CA, Bhatia SK. Effect of the CaO sintering on the calcination rate of $CaCO_3$ under atmospheres containing CO_2. AIChE J 2018;64(10):3638–48. https://doi.org/10.1002/aic.16326.
[29] Bogdanović B, Reiser A, Schlichte K, Spliethoff B, Tesche B. Thermodynamics and dynamics of the Mg–Fe–H system and its potential for thermochemical thermal energy storage. J Alloys Compd 2002;345(1–2):77–89. https://doi.org/10.1016/S0925-8388(02)00308-0.
[30] Ammendola P, Raganati F, Landi E, Natali Murri A, Miccio F. Kinetics of the carbonation reaction of an SrO-Al_2O_3 composite for thermochemical energy storage. Chem Eng J 2021;420:129618. https://doi.org/10.1016/j.cej.2021.129618.
[31] Gigantino M, Kiwic D, Steinfeld A. Thermochemical energy storage via isothermal carbonation-calcination cycles of MgO-Stabilized SrO in the range of 1000–1100 °C. Sol Energy 2019;188:720–9. https://doi.org/10.1016/j.solener.2019.06.046.
[32] Sheppard DA, Paskevicius M, Javadian P, Davies IJ, Buckley CE. Methods for accurate high-temperature Sieverts-type Hydrogen measurements of metal hydrides. J Alloys Compd 2019;787:1225–37. https://doi.org/10.1016/j.jallcom.2019.02.067.
[33] Lemmon E, Huber M, McLinden M. NIST standard reference database 23: reference Fluid thermodynamic and Transport properties-REFPROP. 2013., Version 9.1. https://tsapps.nist.gov/publication/get_pdf.cfm?pub_id=912382.
[34] Perl J, Shin J, Schumann J, Faddegon B, Paganetti H. TOPAS: an innovative Proton Monte Carlo Platform for research and clinical applications. Med Phys 2012;39(11):6818–37. https://doi.org/10.1118/1.4758060.
[35] Wallwork KS, Kennedy BJ, Wang D. The high-resolution powder diffraction beamline for the Australian synchrotron. AIP Conf Proc 2007;879(February 2007):879–82. https://doi.org/10.1063/1.2436201.

[36] Bagherisereshki E, Tran J, Lei F, AuYeung N. Investigation into SrO/$SrCO_3$ for high temperature thermochemical energy storage. Sol Energy 2018;160(December 2017):85–93. https://doi.org/10.1016/j.solener.2017.11.073.
[37] Ptáček P, Bartoníčková E, Švec J, Opravil T, Šoukal F, Frajkorová F. The kinetics and Mechanism of thermal decomposition of $SrCO_3$ Polymorphs. Ceram Int 2015; 41(1):115–26. https://doi.org/10.1016/j.ceramint.2014.08.043. Part A).
[38] Jacob K, Rajitha G. Thermodynamic properties of strontium titanates: Sr_2TiO_4, $Sr_3Ti_2O_7$, $Sr_4Ti_3O_{10}$, and $SrTiO_3$. J Chem Therm 2011;43:51–7. https://doi.org/10.1016/j.jct.2010.08.011.
[39] Pitt MP, Paskevicius M, Webb CJ, Sheppard DA, Buckley CE, Gray E. MacA. The synthesis of Nanoscopic Ti based alloys and their effects on the MgH2 system compared with the $MgH_2 + 0.01Nb_2O_5$ Benchmark. Int J Hydrogen Energy 2012; 37(5):4227–37. https://doi.org/10.1016/j.ijhydene.2011.11.114.
[40] Roine A. HSC Chemistry® [Software] 2018. Software available at: www.outotec.com/HSC.
[41] Carrillo AJ, Gonza J, Romero M, Coronado JM. Solar energy on demand : a review on high temperature thermochemical heat storage systems and materials. 2019. https://doi.org/10.1021/acs.chemrev.8b00315.
[42] Medina-Carrasco S, Valverde JM. The Calcium Looping process for energy storage: insights from in situ XRD analysis. Chem Eng J 2022;429(June 2021):132244. https://doi.org/10.1016/j.cej.2021.132244.
[43] Srivastava D, Norman C, Azough F, Schäfer MC, Guilmeau E, Freer R. Improving the Thermoelectric properties of $SrTiO_3$-based Ceramics with Metallic inclusions. J Alloys Compd 2018;731:723–30. https://doi.org/10.1016/j.jallcom.2017.10.033.
[44] Fumega AO, Fu Y, Pardo V, Singh DJ. Understanding the Lattice thermal conductivity of $SrTiO_3$ from an ab Initio perspective. Phys Rev Mater 2020;4(3): 033606. https://doi.org/10.1103/PhysRevMaterials.4.033606.
[45] National Minerals Information Center. U.S. Geological Survey Mineral Commodity Summaries 2022 Data Release; 2022. https://doi.org/10.5066/P9KKMCP4.
[46] Steel,Aluminum,Nickel,Rare earth,new energy,Copper Prices Charts and news-Shanghai Metals Market. https://www.metal.com/(accessed 2023-December-19)..
[47] Manickam K, Mistry P, Walker G, Grant D, Buckley CE, Humphries TD, Paskevicius M, Jensen T, Albert R, Peinecke K, Felderhoff M. Future perspectives of thermal energy storage with metal hydrides. Int J Hydrogen Energy 2019;44(15): 7738–45. https://doi.org/10.1016/j.ijhydene.2018.12.011.